Numerical Simulations of Combustion Processes in Hybrid Rocket Engines Using OpenFoam and COOLFluiD Codes

L. Merotto⋆ and A. Mazzetti⋆⋆
⋆Aerospace Sciences and Technology Department, Politecnico di Milano
via La Masa 34, 20156 Milano - Italy. Mail: laura.merotto@polimi.it
⋆⋆Mathematics Department, Politecnico di Milano
Piazza Leonardo da Vinci 32, 20133 Milano - Italy

Abstract

The aim of this work is to contribute to hybrid technology improvement by providing a reliable numerical simulation of processes occurring in the combustion chamber of a hybrid rocket engine (HRE). Numerical simulations are particularly useful for the investigation of variations such as O/F ratio change during combustion, local variations due to different boundary layer thickness and transient phenomena associated to the motor throttling, which are of major importance for HRE. The numerical simulation of reacting flow field is performed in different combustion chamber geometries. The results presented include the investigation of several major parameters variation effects on the global flow field.

1. Introduction

1.1 CFD Modeling of Hybrid Rocket Engines

Hybrid rocket combustion flowfields involve fluid-dynamics coupled with combustion, turbulence, radiation, spray atomization, vaporization (if liquid oxidizers are used), fuel surface pyrolysis (if polymer-based fuels such as HTPB are used), and liquid fuel films (if liquefying fuels, such as paraffins, are used). Several approaches have been proposed for multiphase flowfields in the literature, including Eulerian-Eulerian homogeneous mixture formulation, Eulerian-Eulerian multifluid formulation, and Eulerian- Lagrangian approaches.
Analytical investigations of hybrid rocket combustion have usually been based on the classical boundary-layer analysis of Marxman et. al. [1] to determine the heat flux to the fuel surface and consequently the surface regression rate. Typically, the regression rate is given by simple correlations such as $r_b = G_0^n$, where G_0 is the head end specific flow rate of the oxidizer and n is generally in the range 0.6-0.8. However, such simplified correlations cannot account for all the variations in operating conditions, chamber pressure, radiation, and finite-rate chemical kinetics. Some of these effects were characterized experimentally by Chiaverini et. al. [2], who also proposed a more complete model, which includes terms accounting for radiative fluxes. Nevertheless, such simplified models are limited to providing qualitative trends and are not adequate to give quantitative data.
Cheng et. al. [3] developed a model for hybrid rocket flowfields which solved the three-dimensional Reynolds averaged Navier-Stokes equations within a Lagrangian-Eulerian framework. Lagrangian droplet tracking was used to describe the motion and vaporization of the liquid oxygen droplets, and gave the source terms for the vaporized fuel in the Eulerian gas-phase equations. In [3], the authors successfully computed the 3D flowfield in two practical motor configurations and several simplified port configurations. Lin and Chiu [4] developed an Eulerian-Eulerian spray combustion model for hybrid rocket flowfields, focused on the post-atomization conditions prevailing in the downstream portion of the spray. Computational results were validated with experimental data, and parametric effects of droplet size and velocity distributions, as well as oxidizer flow rate on fuel regression and combustion efficiency, were performed.
In recent years, Venkateswaran [5] developed a computational model for hybrid rocket flowfields simulation. The model uses the complete time-dependent Navier-Stokes equations, coupled to auxiliary transport equations and physical submodels, and includes the effects of finite-rate chemistry, turbulence, gas-phase radiation, and coupling between gas and solid phases. The focus of [5] is the characterization of the fuel regression rate by comparing and calibrating the data using the experimental results by Chiaverini and co-workers [2], [6]. All the computational results shown in [5] are two-dimensional and obtained using a quasi-steady assumption, *i.e.* the fuel port dimensions were held fixed at values corresponding to different burning stages, and steady-state solutions were obtained to provide the instantaneous

burning rates at the operating conditions. The quasi-steady assumption is adequate because the fuel surface regression rate is typically much smaller than the axial velocity in the port. In conclusion, it can be observed that even if many interesting (mostly qualitative) results were obtained so far, the use of CFD to model hybrid rocket flowfields need to be improved. In particular, further investigation is needed in order to model multiphase flows, turbulence, solid- and gas-phase interface combustion, and radiation.

A recent study by Coronetti and Sirignano [7] predicts the regression rate of the Hydroxyl -Terminated Poly-Butadiene (HTPB)/ Gaseous Oxygen formulation and its sensitivities to some operating parameters, such as combustion chamber pressure, oxygen inlet temperature, and mass flow rate. Furthermore, an analysis of other variables is used to explain the experimentally observed regression rate behavior. Particular emphasis is placed on the effect of the oxygen between the flame and the surface, which is considered responsible for the pyrolysis process enhancement.

This work is aimed to give a contribution to a CFD reliable simulation of the combustion processes involved in hybrid rocket engines. The numerical simulation of HTPB combustion processes in a hybrid rocket engine combustion chamber is presented in this work. Simulations were carried out on different chamber geometries and using two different numerical codes. This investigation is a first step in a wider project, aimed to two main results. The first one is to simulate the combustion processes of liquefying (paraffin-based) fuels for hybrid propulsion, which requires the simulation of a spray combustion. Furthermore, a moving mesh is needed in order to adequately simulate the regression of the solid fuel. The mesh motion needs to be linked to the effective solid fuel regression rate, which in turn is dependent on the imbalance at the solid-gas interface. The second objective is to validate the numerical code with experimental results obtained in a *ad hoc* test rig at Space Propulsion Laboratory of Politecnico di Milano. Work is ongoing to design and set up the test rig, and the numerical simulation on several different geometries is used to define a feasible geometry for the actual combustion chamber to be designed for experimental validation. The fuel configuration chosen for this work is a slab geometry, which allows an easier optical access for experimental tests video-recording. In order to achieve the aforementioned objectives, a preliminary study was performed and is reported in this work. Simulation of the combustion processes of HTPB in a 2D slab hybrid rocket combustion chamber and investigation of the effect of different operating parameters were performed. The main results of this preliminary investigation are reported in the following sections of this paper.

1.2 Numerical model and codes used

The model used in the present work solves the governing equations for a turbulent, multi-species reacting flow. In order to avoid explicit modeling of fluctuation correlations, such as $\overline{\rho' u'}$, which appear in *time-averaging* techniques (RANS), *Favre-averaging* (or *mass-averaging*) for such equations will be introduced. The complete set of equations used can be found in [8]. The closure for turbulent energy transport is based on $C_p \nabla T$, following [9] and [10]. The numerical codes used in this work are OpenFoam and COOLFluiD. OpenFoam is an open-source finite-volume code for computational fluid-dynamics [11]. For the OpenFoam code simulations in this work, reactingFoam solver for laminar or turbulent RANS flow of compressible fluids with chemical reactions was used. Preconditioned conjugated gradient methods were applied for ρ and p governing equations; preconditioned bi-conjugate gradient solver using a run-time selectable preconditioner were used for U, k and ϵ solutions. The merged PISO-SIMPLE (semi-implicit method for pressure-linked equation) algorithm (PIMPLE) algorithm was used for transient simulations. The SIMPLE algorithm calculates pressure on a staggered grid from velocity components by applying an iterative procedure coupled with the Navier-Stokes equations, while the PIMPLE algorithm combines the SIMPLE algorithm with PISO algorithm (pressure implicit with splitting the operators) to correct both velocities and pressure explicitly. The combustion model is the Chalmers PaSR model [12]. The OpenFoam release used for this work is version 2.1.

The COOLFluiD scientific computing environment, developed at von Kàrman Institute for Fluid Dynamics, is an MPI parallel code, constituted by a kernel plus dynamic plugins structure. This code applies a space second order cell-centered finite volume method for the solution of Navier-Stokes system of equations, with Liou AUSM+-Up flux-splitting upwinding technique. The linear system is solved using PETSc libraries with Generalized Minimum Residual (GMRES) technique. A description of the code can be found in [8].

2. Results discussion

2.1 Domain geometries and case set up

In the first part of this work, some cold tests were performed (not reported here), in order to assess the feasibility of the fluid-dynamic flow field simulation of the numerical code used. In the second part, chemical reactions were activated. The work is mainly aimed to the development of a new combustion chamber for experimental tests in

the framework of hybrid rocket engines combustion processes investigation. Therefore, preliminary studies included numerical simulations on several different geometries. Three geometries are presented in this work, and are called CF2, CF6 and CF8. The first computational domain, CF2, is a simple rectangular combustion chamber, as shown in Figure 1. The oxygen inlet is in the left part of the combustion chamber; the fuel inlet is on the bottom part, 25 *mm* from the left edge. The outlet patch corresponds to the whole right patch.

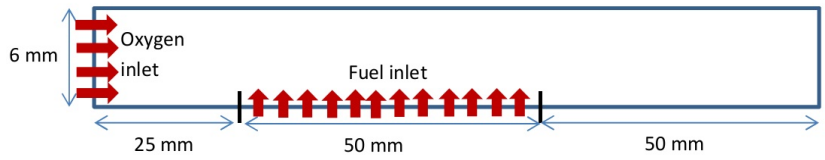

Figure 1: Computational domain used for CF2 geometry.

The second and third computational domain (CF6 and CF8) are shown in Figure 2 and 3, respectively. CF6 has a backward facing step, and a narrowing post-chamber. The oxygen inlet is the whole left patch of the domain, while the outlet is the right patch. The fuel sample length is 50 *mm*. This geometry is close to the geometry of an experimental combustion chamber, but steep change of slopes can result in too high vorticity.

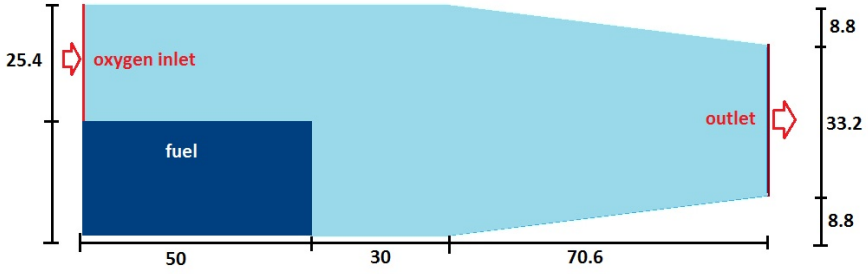

Figure 2: Computational domain used for CF6 geometry. Dimensions in *mm*.

The CF8 geometry main characteristic is the trapezoidal fuel, which avoids steep steps in the computational domain. In this case, the inlet and outlet regions are smaller than the corresponding patch, as shown in Figure 3, and are equal to the diameter of standard pipelines for inlet/outlet that can be used in the actual combustion chamber.

For all tests, a no-slip condition for velocity was imposed on walls. A Neumann condition was imposed on the outlet patch.

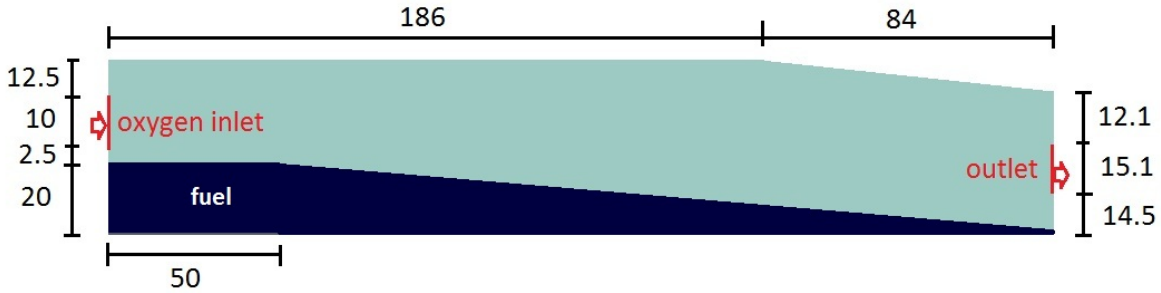

Figure 3: Computational domain used for CF8 geometry. Dimensions in *mm*.

A six-step reaction model for butadiene combustion is implemented, which assumes gaseous butadiene to be the only pyrolisis product of butadiene [13] and uses Arrhenius type reaction constants. The kinetic model is shown in Table 1.

Table 1: Six-step reaction mechanism. Activation energies are in $cal/molK$.

Reaction	**Coefficients**
$C_4H_6 + 2O_2 \Rightarrow 4CO + 3H_2$	R=$3.79*10^{11}\left(\frac{-30000}{RT}\right)[C_4H_6]^{0.5}[O_2]^{1.25}$
$C_4H_6 + 4H_2O \Rightarrow 4CO + 7H_2$	R=$3.08*10^{8}\left(\frac{-30000}{RT}\right)[C_4H_6][O_2]$
$CO + H_2O \Leftrightarrow CO_2 + H_2$	R=$2.75*10^{9}\left(\frac{-20000}{RT}\right)[CO][H_2O]$
$H_2 + 0.5O_2 \Leftrightarrow H_2O$	R=$7.50*10^{15}\left(\frac{-40000}{RT}\right)[H]^{0.25}[O_2]^{1.5}$
$O_2 \Leftrightarrow 2O$	R=$1.50*10^{9}\left(\frac{-113000}{RT}\right)[O_2]$
$H_2O \Leftrightarrow OH + H$	R=$2.30*10^{22}\left(\frac{-120000}{RT}\right)[H_2O]$

2.2 Reacting case: CF2 geometry

Single- and double-slab simulations were performed. The following initial conditions are used: oxidizer inlet velocity is set to $V_{ox} = 6\ m/s$ (axial direction), fuel inlet velocity $V_F = 0.26\ m/s$ (vertical direction, from bottom to top), oxidizer inlet temperature are set to 300 K, whereas fuel inlet temperature is set to 1500 K in order to ensure ignition. Walls temperature is set to 600 K for lower walls, 300 K for upper wall. The temperature distribution obtained is shown in Figure 4. At the beginning of the calculation, the combustion chmaber contains only inert species (N_2). At $t = 0\ s$, the fuel and oxidizer start flowing in the combustion chamber. The combustion initiation takes place at about 5 ms, where a first nucleus of combustion is visible. Stabilization of the temperature distributions is achieved after 15 ms of simulated time. The temperature distribution obtained for the double-slab case is shown in Figure 5. The fuel grain position is also indicated, for clarity. In this case, $V_F = 0.26\ m/s$ is directed from bottom to top for the bottom slab, and in the opposite direction for the upper slab.

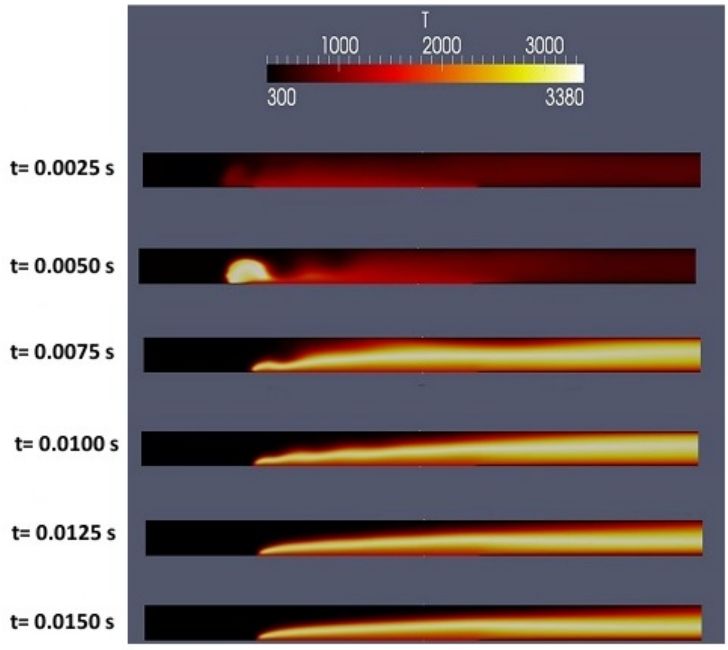

Figure 4: Temperature distribution for single slab configuration, at different time steps.

Temperature distribution and axial velocity distribution vs. y distance are shown in Figures 6 and 7 for the single-slab case, and in Figures 8 and 9 for the double-slab case. The longitudinal locations selected for data sampling are 50, 75, 95 and 120 mm, corresponding to 50% fuel grain length, fuel end-end middle post-chamber and end of post-chamber location, respectively. It can be seen that the peak temperature is around 3460 K for both single- and double-slab configuration. If the flame location is approximately identified with the peak temperature, it can also be noticed that single-slab configuration results in a higher flame height (about 2 mm) when compared to the double-slab

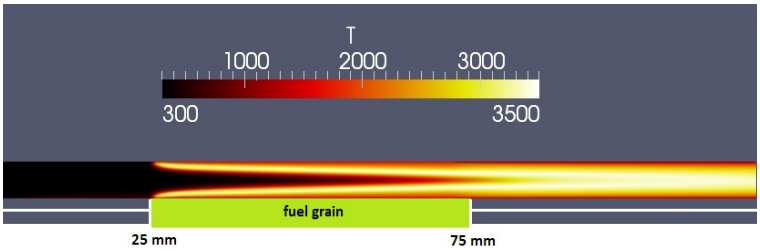

Figure 5: Temperature distribution for double-slab configuration. Time 1 s.

configuration, in which both flames are about 1.4 mm thick. An interesting observation arises examining the axial velocity distribution for the two configurations (Figures 7 and 9). In the post-chamber axial location $x = 120$ mm, the peak axial velocity is less than 70 m/s for the single-slab configuration, while it is about 120 m/s for the double-slab configuration. This indicates that double-slab configuration results in higher flow acceleration.

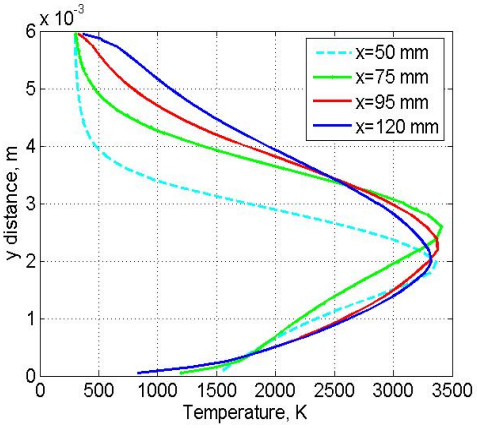

Figure 6: Temperature distribution vs. y distance for single-slab configuration, at different x locations. Time 1 s. Geometry: CF2.

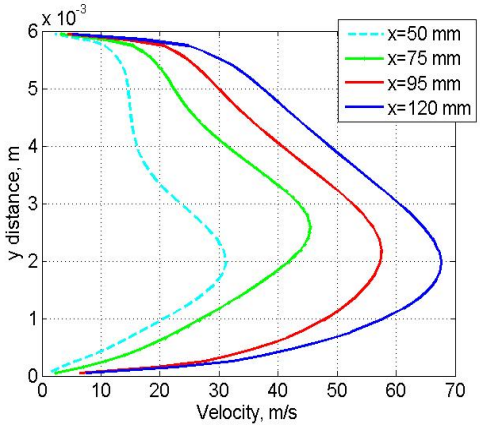

Figure 7: Axial velocity distribution vs. y distance for single-slab configuration, at different x locations. Time 1 s. Geometry: CF2.

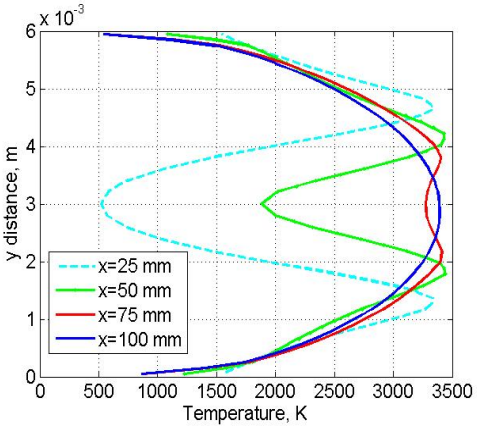

Figure 8: Temperature distribution vs. y distance for double-slab configuration, at different x locations. Time 1 s. Geometry: CF2.

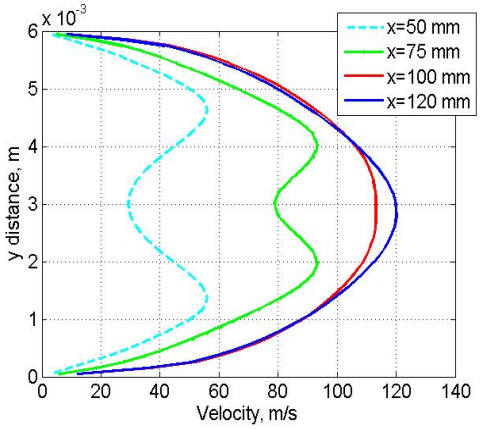

Figure 9: Axial velocity distribution vs. y distance for double slab configuration, at different x locations. Time 1 s. Geometry: CF2.

These results are useful for the experimental test rig design. In fact, predicting the axial velocity in the combustion chamber allows calculating the oxidizer mass flux, which in turn is known to affect the overall regression rate. Experimental data obtained in a similar combustion chamber [14] show that for an oxygen mass flux of 120 $kg/m^2 s$ (corresponding to 100 m/s oxygen axial velocity in the combustion chamber tested), the HTPB regression rate measured is about 0.25 mm/s for single slab configuration, and about 0.4 mm/s for double slab configuration.

2.3 Reacting case: CF6 geometry

A parametric investigation was performed, changing the oxidizer inlet velocity, the fuel inlet velocity, and the oxidizer inlet temperature. Figure 10 shows the temperature distribution for different oxidizer inlet velocity, ranging from 5 to 30 m/s. Results show that for increasing oxidizer inlet velocity from 5 to 15 m/s, the flame position moves downstream. When the oxidizer inlet velocity is at least 20 m/s, a turbulent combustion takes place. A flame position moving downstream is visible also in Figure 11, where the effect of increasing fuel inlet velocity is investigated. When the ratio between V_{ox} and V_F decreases, the flame also shifts in the positive y direction. The flame position shifts downstream also for decreasing oxidizer inlet temperature (figure not shown). For $T_{ox} = 500\ K$ the flame moves beyond the end of the post-chamber, while for $T_{ox} = 450\ K$ no ignition takes place.

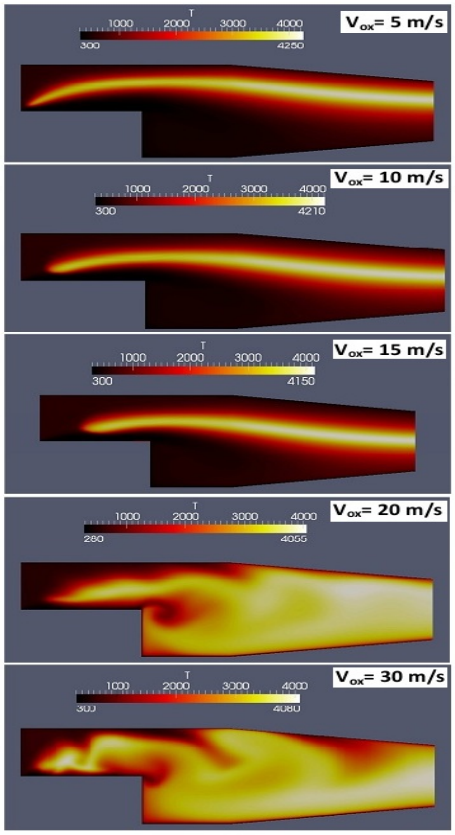

Figure 10: Temperature distribution for different oxidizer inlet velocity, at $t = 0.1\ s$. Geometry: CF6.

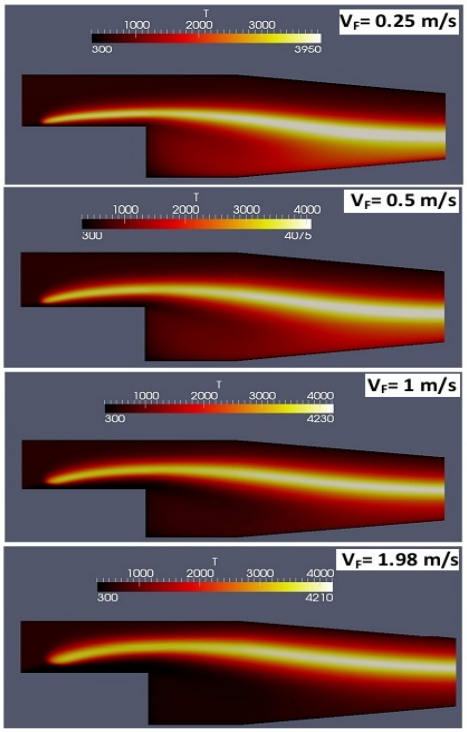

Figure 11: Temperature distribution for different fuel inlet velocity, at $t = 0.1\ s$. Geometry: CF6.

Figure 12 (left) shows the temperature distribution for different oxidizer inlet velocity V_{ox}, at longitudinal location $x_1 = 29.4\ mm$, corresponding to the fuel sample end. Figure 12 (right) shows the temperature distribution for different fuel inlet velocity V_F, at x_1 location. Results are plotted for $t = 0.1\ s$. Examining Figure 12, it can be noticed that for inlet velocities up to 15 m/s the flame height (maximum temperature) tends to decrease for increasing inlet velocity. Nevertheless, when V_{ox} is higher, a different trend is displayed, reflecting the disordered behavior shown in Figure 10. Similar results are obtained for sampling at different longitudinal locations (not reported here). Flame height increases with increased fuel inlet velocity, as shown in Figure 12 (right). In this case, no irregular behavior is displayed.

2.4 Reacting case: CF8 geometry

The case was run both in reacting and non-reacting conditions. In both reacting and non-reacting cases, the initial conditions are set to the same values used for case CF2 ($V_{ox} = 6\ m/s$ and $V_F = 0.26\ m/s$). The fuel is introduced at a constant velocity from both the horizontal and the sloping fuel surfaces. Operating pressure is 1 bar. Moreover, the fuel horizontal length (L_H) was changed to $L = 100\ mm$ (case CF8b) and $L = 150\ mm$ (case CF8c), in order to investigate the effect of different fuel grain size on the overall temperature and velocity distribution. The initial conditions for each

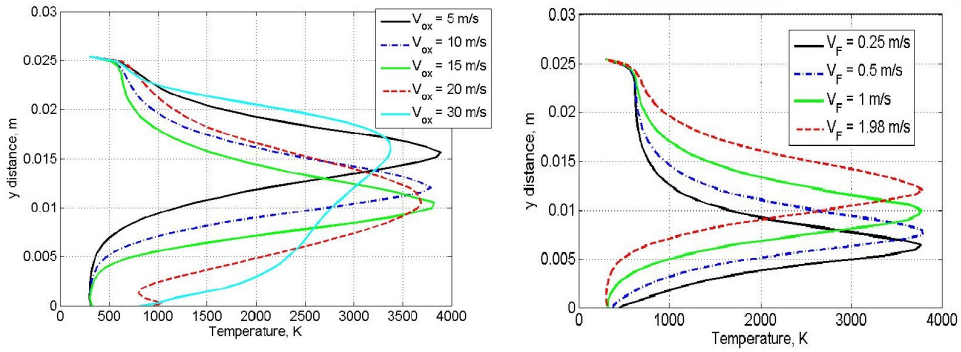

Figure 12: Temperature distribution for different oxidizer inlet velocity (left) and for different fuel inlet velocity (right), at $t = 0.1\ s$. Geometry: CF6.

case run are shown in Table 2. The O/F value is obtained from:

$$\frac{O}{F} = \frac{\rho_{ox} V_{ox} A_{ox}}{\rho_F V_F A_F} \tag{1}$$

where ρ is the density (kg/m^3), V is the velocity (m/s) and A is the fuel area (m^2), obtained taking into account both the horizontal and the sloping surfaces.

Table 2: Initial conditions for the case with CF8 geometry.

case	O/F	L_H	**inlet velocity**	**inlet temperature**	**chemical reactions**
		mm	m/s	K	
CF8	2.8	50	$V_{ox} = 6$	$T_{ox} = 300$	*no*
			$V_F = 0.26$	$T_F = 1500$	
CF8r	2.8	50	$V_{ox} = 6$	$T_{ox} = 300$	*yes*
			$V_F = 0.26$	$T_F = 1500$	
CF8b	2.8	100	$V_{ox} = 6$	$T_{ox} = 300$	*no*
			$V_F = 0.26$	$T_F = 1500$	
CF8rb	2.8	100	$V_{ox} = 6$	$T_{ox} = 300$	*yes*
			$V_F = 0.26$	$T_F = 1500$	
CF8c	2.8	150	$V_{ox} = 6$	$T_{ox} = 300$	*no*
			$V_F = 0.26$	$T_F = 1500$	
CF8rc	2.8	150	$V_{ox} = 6$	$T_{ox} = 300$	*yes*
			$V_F = 0.26$	$T_F = 1500$	
CF8rd	2.8	50	$V_{ox} = 20$	$T_{ox} = 300$	*yes*
			$V_F = 0.26$	$T_F = 1500$	

Figure 13 shows the temperature distribution for the three CF8 cases, having L_H of 50, 100 and 150 mm, respectively. The axial location corresponding to the upper wall slope change (186 mm) is also indicated for clarity.

A comparison between the longitudinal velocity u_x was performed in different axial locations. Figure 14 shows the longitudinal velocity vs. chamber section for axial locations corresponding to 25 mm and 50 mm, for the case with $L_H = 50\ mm$. The y section corresponding to fuel horizontal surface is -0.005 m. It can be observed that chemical reactions result in a dramatic longitudinal velocity increase, particularly in the flame zone over the fuel surface. Examining Figure 14, it can be seen that chemical reactions result in an enhanced axial velocity, particularly in the flame zone over the fuel surface. When chemical reactions occur, the peak velocity is around 11.5 m/s, almost twice the peak velocity for the non-reacting case, due to the combustion products expansion. Moreover, this peak is lower in the reacting case (about 5 mm over the fuel surface) than in the non-reacting case (about 15 mm over the fuel surface). The U_x increase becomes more pronounced moving downstream: at $x = 93\ mm$ from the head-end, the U_x increase is 5.4 times (1.52 m/s for the non-reacting case and 8.21 m/s for the reacting case). The same effect occurs for the cases with $L_H = 100\ mm$ and $L_H = 150\ mm$.

It is also interesting to examine the effect of the fuel grain length on the axial velocity distribution, reported in Figure 15, left part. The non-reacting cases display all the same maximum axial velocity. On the other hand, the

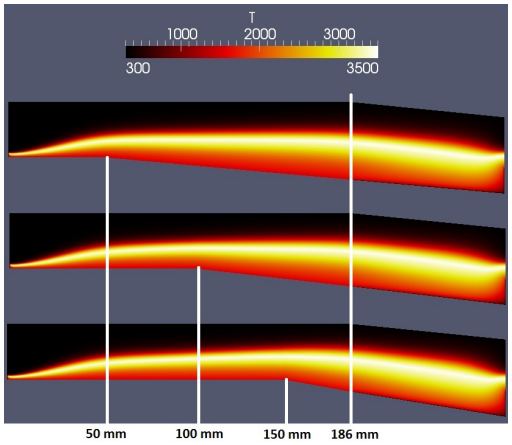

Figure 13: Temperature distribution for CF8 case, (50 *mm* grain length) (top), for CF8b case (100 mm grain length)and for CF8c case (150 *mm* grain length). Time 0.2 *s*.

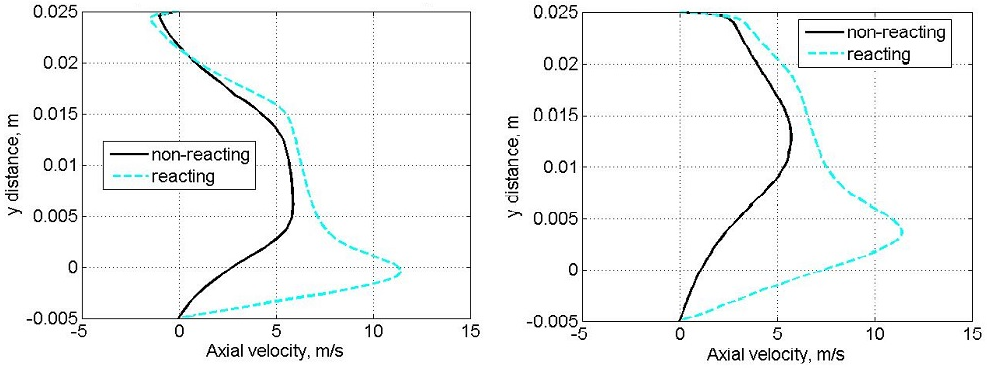

Figure 14: Axial velocity distribution for axial locations $x_1 = 25$ *mm* (left) and $x_2 = 50$ *mm* (right). Time 0.2 *s*.

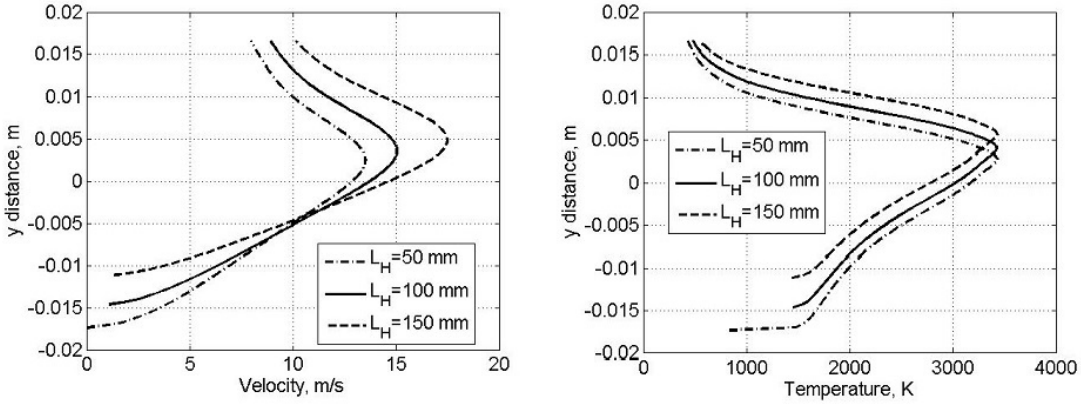

Figure 15: Axial velocity distribution (left) and temperature distribution (right) for reacting CF8 cases. Axial location: 186 *mm*. Time: 0.2 *s*.

reacting cases (Figure 15) show that the maximum axial velocity increases with increasing L_H: the three maximum axial velocity values are 13.5, 15.1 and 17.5 m/s. The effect of fuel grain length on temperature distribution is shown in Figure 15, right part. The values are referred to an axial position of 186 *mm* (post-chamber), at 0.2 s of simulated time. It can be seen from the results reported that the maximum temperature reached in all the CF8 cases is the same (about 3460 K); nevertheless, the position of this maximum along the y axis, which is roughly the flame position, is different in the three cases, namely the flame height is increasing with increasing horizontal fuel length L_H. The three flame positions are 2.9 *mm* for $L_H = 50$ *mm*, 4 *mm* for $L_H = 100$ *mm*, and 5.6 *mm* for $L_H = 150$ *mm*.

The species mass fraction distribution at $x = 186$ *mm* is shown in Figure 16 for the case with horizontal fuel length of 50 *mm*.

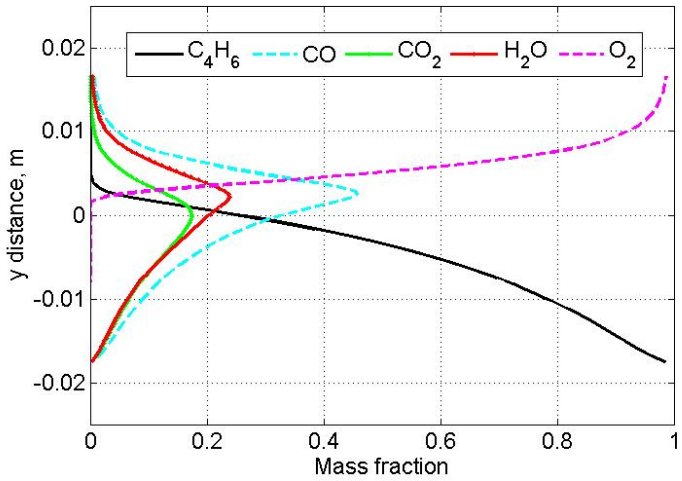

Figure 16: Species mass fraction distribution for reacting CF8 case with $L_H = 50$ *mm*, at $x = 186$ *mm*. Time: 0.2 s.

When a higher oxygen inlet velocity is imposed ($V_{ox} = 20$ m/s), temperature and velocity distribution do not change with respect to the lower V_{ox} tests shown. In particular, the re-circulation visible in CF6 cases is absent, because no steep change of slope disturbs the flow. Figure 17 shows a comparison between the two cases having different oxygen inlet velocity, in terms of temperature and axial velocity vs. y section, at an axial location $x = 186$ *mm*. On the basis of the presented results, the CF8 geometry was selected for further tests because it allows obtaining a regular behavior of the flowfield. In particular, work is ongoing in order to design and setup an experimental combustion chamber for code validation based on *ad hoc* tests.

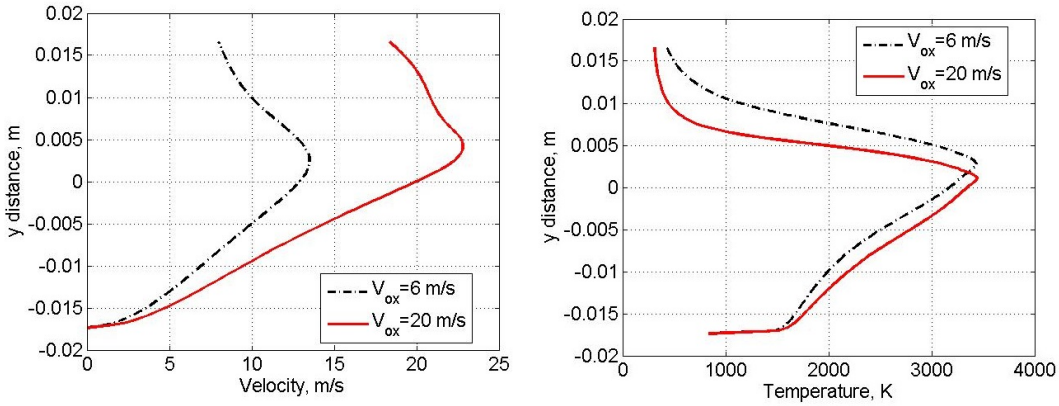

Figure 17: Axial velocity distribution (left) and temperature distribution (right) for reacting CF8 cases having different oxygen inlet velocity. Axial location: 186 *mm*. Time: 0.2 s.

2.5 CF2 geometry: COOLFluiD code results

The results obtained so far are a preliminary investigation aimed to the ambitious project of simulating the spray combustion of paraffin fuels in a moving domain. Before starting the code re-programming, it is interesting to compare the results obtained using an OpenFoam tutorial solver with an *ad hoc* solver developed with the aim to overcome the limits of the existing codes for polymer combustion simulation. For this reason, the results obtained for the CF2 geometry were compared to results obtained using COOLFluiD [8].

Figures 18 and 19 report the temperature distribution and the axial velocity distribution, respectively, obtained with COOLFluiD code. Figure 20 reports the temperature distribution in the combustion chamber obtained for double slab configuration.

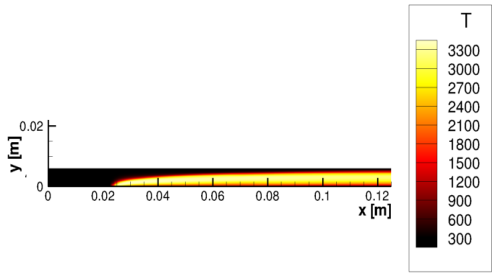

Figure 18: Temperature distribution. COOLFluiD simulation.

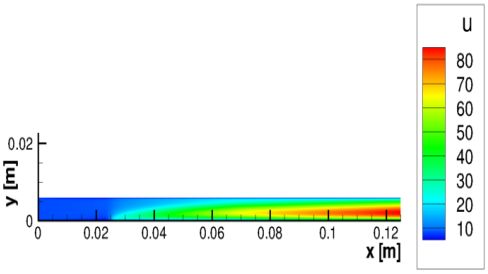

Figure 19: Axial velocity distribution. COOLFluiD simulation.

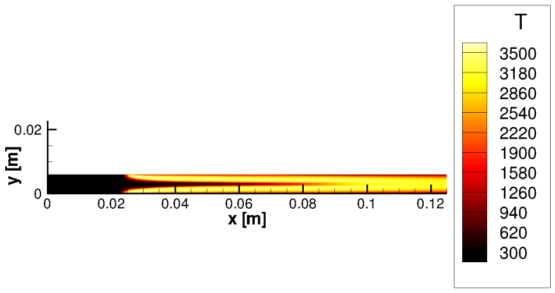

Figure 20: Temperature distribution for CF2 geometry, double slab configuration. COOLFluiD simulation.

Sampling of temperature, axial velocity, and species distribution was performed for both COOLFluiD and OpenFoam simulations. The longitudinal sections selected for sampling are 50 *mm* (corresponding to 50% sample length), 75 *mm* (sample end), 90 *mm* (post-chamber) 120 *mm* (end of post-chamber).

Temperature and axial velocity distribution vs. *y* distance are shown in Figures 21 and 22, respectively, for single slab configuration, and in Figures 23 and 24, respectively, for double slab configuration.

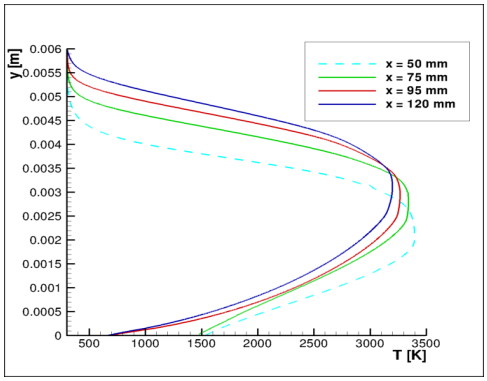

Figure 21: Temperature distribution vs. *y* distance. COOLFluiD simulation.

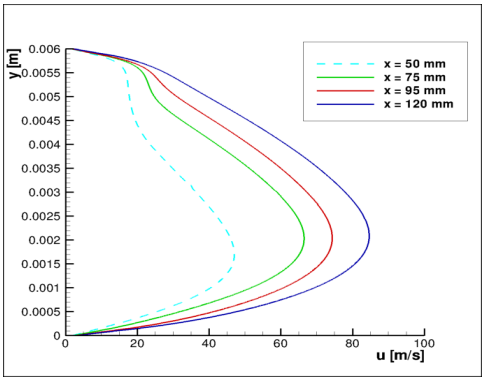

Figure 22: Axial velocity distribution vs. *y* distance. COOLFluiD simulation.

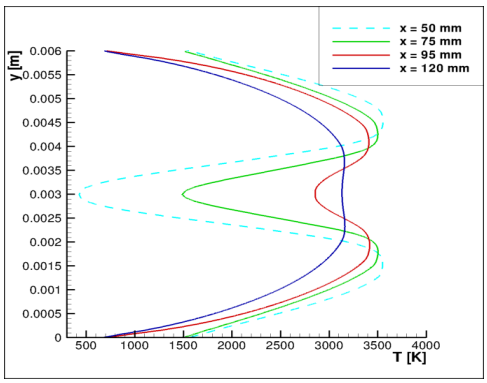

Figure 23: Temperature distribution vs. y distance. COOLFluiD simulation, double slab configuration.

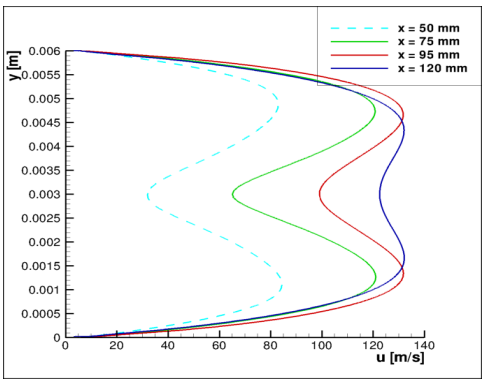

Figure 24: Axial velocity distribution vs. y distance. COOLFluiD simulation, double slab configuration.

Species mass fraction distribution vs. y distance were obtained (not reported here). Similar distributions are obtained when comparing the reactants mass fractions, C_4H_6 and O_2, thus confirming the boundary conditions are correctly settled. Comparing the H_2O mass fraction distribution obtained with the two codes, it can be seen that the maximum mass fraction obtained is around 0.21-0.23 for both codes, even if the computed mass fraction with OpenFoam is higher. On the other hand, CO_2 mass fraction is higher for COOLFluiD computations, because there is more dissociation due to the multi-time PaSR used.

In conclusion, the results obtained with OpenFoam can not be directly compared to the COOLFluiD results, because there are some differences in the computation. The different turbulence model used and the modelling of turbulent energy transport terms [8], together with the multi-time PaSR used in COOLFluiD, lead to some differences in velocity and temperature distribution, and in turn in the chemical species distribution. Nevertheless, these difference are minor, and the global trends are the same.

3. Conclusions

A preliminary numerical investigation of the combustion processes occurring in a hybrid rocket engine combustion chamber was performed in the framework of a wider project aimed to compare numerical and experimental results on both traditional and innovative (liquefying) solid fuels. In this first phase, different chamber geometries and the effect of several operating parameters were investigated using a transient OpenFoam solver for reacting flows. A six-reactions kinetic scheme for HTPB combustion was implemented in this work.

Results are presented for three different chamber geometries. The temperature and axial velocity distributions in different chamber sections are analyzed, and the effect of different operating parameters is discussed.

Results show that double-slab fuel configuration, when compared with single-slab, results in increased axial velocity (almost double). An increased in oxygen and/or fuel inlet velocity result in a shifting of the flame zone and in decreased flame thickness. When the ratio between oxygen and fuel inlet velocity is such that a fully turbulent flow is obtained, an irregular behavior is displayed by the temperature and velocity distribution if a domain with a backward-facing step is used. Also the fuel geometry affects the overall distributions in the combustion chamber, determining higher axial velocities and higher flame heights with increasing fuel lengths.

On the basis of the results obtained, a geometry was selected for further investigation, and will be used to design and set up a combustion chamber to be used for code validation.

The obtained results were compared to similar computations performed with a different code (COOLFluiD), showing that the overall trends are similar.

4. Further developments

Work is ongoing in order to adjust OpenFoam and COOLFluiD simulation parameters in order to obtain identical conditions, and compare the codes accuracy and computational times.

In order to achieve a reliable simulation of the whole experimental case, several improvements are needed, namely: a moving mesh in the zone of the regressing solid fuel; an energy balance at the solid-gas interface, able to correctly simulate the pyrolysis of the solid fuel and the interaction with the gas phase; and a mesh movement based on the regression velocity computed at the interface.

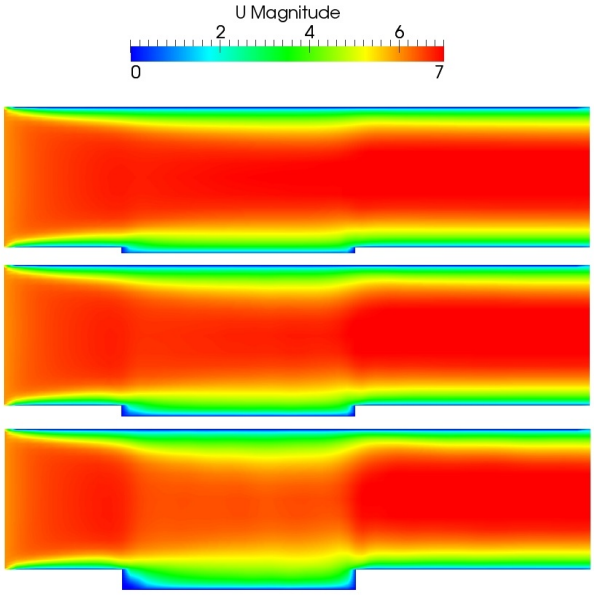

Figure 25: Moving mesh preliminary simulation. Flowfield in the combustion chamber for different time steps.

A preliminary simulation with a moving mesh is reported as an example in Figure 25. The increasing depth of the step caused by fuel regression is clearly visible. In order to do this, a new computational domain is implemented, and a new solver based on the PIMPLE standard solver for compressible fluids is being set up, with a moving mesh algorithm [15], [16] for fuel regression. Moreover, since paraffin-based fuels are very promising innovative fuels for hybrid propulsion, the simulation of paraffin combustion is needed. Therefore, a spray generation and combustion model will be included.

References

[1] Marxman, G.A., C.E. Woolridge, and R.J. Muzzy. 1964. Fundamentals of hybrid Boundary Layer Combustion. In: *Heterogeneous Combustion, Progress in Astronautics and Aeronautics*, Vol. 15, AIAA, pp. 4854-521.

[2] Chiaverini, M.J., N. Serin, D.K. Johnson, Y.C. Lu, and G.A. Risha. 2000. Regression Rate Behavior of Hybrid Rocket Solid Fuels. In: *Journal of Propulsion and Power*, 16(1), pp. 125-132.

[3] Cheng, G.C., R.C. Farmer, H.S. Jones, and J.S. McFarlane. 1994. Numerical Simulation of the Internal Ballistic of a Hybrid Rocket Motor. In: AIAA Paper 94-0554.

[4] Lin, C.L., and H.H. Chiu. 1995. Numerical Analysis of Spray Combustion in Hybrid Rockets. In: AIAA Paper 95-2687.

[5] Venkateswaran, S. 2007. Computational Fluid Dynamics Modeling of Hybrid Rocket Flowfields. In: *Progress in Astronautics and Aeronautics*, Vol. 218, Fundamentals of Hybrid Rocket Combustion and Propulsion, pp. 323-349.

[6] Chiaverini, M.J., K.K. Kuo, A. Peretz, and G.C. Harting. 2001. Regression Rate and Heat-Transfer Correlations for Hybrid Rockets Combustion. In: *Journal of Propulsion and Power*, Vol.17, No.1, pp. 99-110.

[7] Coronetti, A., and W.A. Sirignano, 2013. Numerical Analysis of Hybrid Rocket Combustion. In: *Journal of Propulsion and Power*, Vol. 29, N. 2, pp. 371-384.

[8] Mazzetti, A., and P. Barbante, 2013. Object Oriented Techniques for the Numerical Simulation of Combustion Processes in Hybrid Rockets. Presented at the 5^{th} *European Conference for Aeronautics and Space Sciences (EUCASS).*

[9] Poinsot, T., and D. Veynante, 2001. Theoretical and Numerical Combustion. RT Edwards Inc. Edition, ISBS I-930217-05-6.

[10] Veynante, D., and L. Vervisch, 2002. Turbulent Combustion Modeling. In: *Progress in Energy and Combustion Science* 28, pp. 193-266.

[11] http://www.openfoam.com/

[12] Golovitchev, V.I. and J. Chomiak. 2001. Numerical Modelling of High Temperature Air Flameless combustion. *4th international symposium on high temperature air combustion and gasification*, Rome, Italy.

[13] Jones, W. P. and R. P. Lindstedt. 1988. Global Reaction Schemes for Hydrocarbon Combustion. In: *Combustion and Flame*, 73:233-249.

[14] Merotto, L. Experimental Investigation of HTPB- and Paraffin-based Fuels Combustion Processes for Hybrid Propulsion. 2011. PhD Dissertation, Aerospace Engineering Department, Politecnico di Milano.

[15] Piscaglia, F., A. Montorfano, and A. Onorati. Towards the LES Simulation of IC Engines with Parallel Topologically Changing Meshes. 2013. In: SAE Int. J. Engines 6(2):926-940. doi:10.4271/2013-01-1096.

[16] Piscaglia, F., A. Montorfano, and A. Onorati. Development of a non-reflecting boundary condition for multidimensional nonlinear duct acoustic computation. 2013. In: Journal of Sound and Vibration, Volume 332, Issue 4, 18 February 2013, Pages 922-935, ISSN 0022-460X, 10.1016/j.jsv.2012.09.030.